Design of Graded Transition Interlayer for Joining Inconel 740H Superalloy with P91 Steel Using Wire-Arc Additive Manufacturing

Soumya Sridar, Xin Wang, Mitra Shabani, Michael A. Klecka, and Wei Xiong

Abstract In this work, two graded transition interlayers were designed using a CALPHAD-based ICME framework (CALPHAD: Calculation of Phase Diagrams; ICME: Integrated Computational Materials Engineering) for joining Inconel 740H superalloy with P91 steel. Successful builds with the designed interlayers (content of P91 steel are 60 and 85 wt.%) sandwiched between the constituent materials were fabricated using wire-arc additive manufacturing. 60% P91 interlayer exhibited an FCC structure with low hardness, while the 85% P91 interlayer had a martensitic structure with high hardness. A two-step post-heat treatment consisting of homogenization at 1150°C and aging at 760°C was designed. 60% P91 interlayer showed no improvement in hardness after aging. It agrees with the CALPHAD modeling that predicts a lack of effective strengthening precipitates at 760°C, whereas the hardness of 85% P91 increased significantly after aging for 8 h due to the precipitation of the $M_{23}C_6$ phase. Mechanical tests equipped with digital image correlation were performed to determine the location of the failure and tensile properties. As-built and heat treated 60% P91 build failed in the graded alloy block, whereas the as-built 85% P91 alloy failed at the 85% P91/740H interface, and the aged alloy failed in the pure P91 region. This proves that post-heat treated 85% P91 is much stronger than pure P91, and the alloy design strategy used in this work proves successful for developing interlayers for dissimilar joining.

Keywords Wire-arc additive manufacturing · Graded interlayer · CALPHAD · ICME · Digital image correlation

S. Sridar · X. Wang · M. Shabani · W. Xiong (✉)
Physical Metallurgy and Materials Design Laboratory, Department of Mechanical Engineering and Materials Science, University of Pittsburgh, Pittsburgh, PA 15261, USA
e-mail: weixiong@pitt.edu

M. A. Klecka
Raytheon Technologies Research Center, 411, Silver Lane, East Hartford, CT 06108, USA

Introduction

In advanced ultra-supercritical (A-USC) powerplant, high operating temperatures (>700°C) and pressures (35 MPa) demands the use of materials with superior creep and oxidation resistance. This led to the development of Inconel 740H superalloy (referred to as 740H hereafter) with a high amount of Cr and Co to attain excellent creep and oxidation properties till 850°C [1], which is expensive. However, there are several regions that operate below 650°C, where the use of 740H superalloys is not required, whereas ferritic-martensitic P91 steel with good creep resistance till 650°C [2] and cheaper than 740H superalloy will be sufficient. The use of different materials in different regions of an A-USC powerplant necessitates the joining of dissimilar materials.

Dissimilar materials can be joined using traditional techniques such as welding [3, 4], brazing [5], or diffusion bonding [6]. In these processes, there are several disadvantages from a process viewpoint, such as long processing time, high production cost, and complex setup with multiple steps involved [7]. From a microstructure standpoint, porosity, crack formation, as well as structural distortion due to the formation of wider heat affected zone (HAZ), are the major drawbacks. In order to overcome these difficulties, additive manufacturing (AM) has become the most sought-after technique to accomplish the joining of dissimilar materials. In an AM process, the component is built layer-by-layer using 3D CAD models [8]. Hence, it has advantages such as freedom to produce complex parts, reduced material wastage, and high efficiency [9].

Several reports are available for multi-material deposition using directed energy deposition (DED)-based systems such as laser engineered net shaping (LENS) using powder as starting material [10–13]. Wire-arc additive manufacturing (WAAM) is another DED-based technique that uses wire as starting material which is melted and deposited using an electric/plasma arc. The high deposition rates in WAAM make it suitable for fabricating large parts that are valuable for real-time applications. Besides, the cost of powders is 2–5 times higher than wire and hence, the materials costs are much lesser for the WAAM process [14]. Owing to these advantages, the WAAM technique will be an appropriate technique for multi-material manufacturing and few reports are available in the literature for using WAAM to join dissimilar aluminum alloys [15, 16], dissimilar steels [17] as well as stainless steel with Ni-base superalloy [18].

Dissimilar joining can be accomplished either by direct bonding of the materials or by introducing an interlayer that leads to a smooth change in composition and properties between the constituent materials. The P91 steel has a martensitic structure, while the 740H superalloy has an γ matrix with FCC structure. Moreover, there is a drastic difference in the coefficient of thermal properties of P91 steel and 740H superalloy. As reported in our previous work [19], when P91 steel was directly bonded over 740H superalloy, cracks formed in the interfacial region and the thermal residual stresses developed due to the differences in thermal properties were relieved by the crack formation. Therefore, the introduction of an interlayer is imperative

to avoid cracking while joining P91 steel with 740H superalloy, and an appropriate interlayer that can ensure a gradual transition between the constituent materials needs to be identified.

In this work, a CALPHAD-based ICME framework (CALPHAD: Calculation of Phase Diagrams; ICME: Integrated Computational Materials Engineering) has been applied to design potential graded alloy compositions that can act as an interlayer between P91 steel and 740H superalloy. Builds with the designed graded alloy interlayer sandwiched between the constituent materials were successfully fabricated using WAAM. The microstructure and mechanical properties of the WAAM builds have been investigated extensively and a suitable post-heat treatment has been designed to remove microstructure inhomogeneities and induce precipitation to improve the properties. This work will prove useful for identifying the graded alloy compositions that can be suitably used as transition interlayers while joining dissimilar materials using any manufacturing technique.

Materials and Methods

Computational Details

In order to identify the compositions that can potentially act as an interlayer, high-throughput thermodynamic calculations were performed using TC-API (Thermo-Calc Application Programming Interface) toolkit known as TC-Python (based on the Python programming language) which is included with the Thermo-Calc software. The content of P91 for the graded alloys was calculated in wt.% and will be expressed as %, hereafter. The fraction of phases at 760°C for different mixtures (101 entries) of P91 steel and 740H superalloy whose compositions were determined by calculating the weighted mean for each element for varying content of P91 steel (in steps of 1%) were calculated. TCNI8, the commercial multicomponent thermodynamic database developed specifically for Ni-base superalloys was used for these calculations. In addition, the Martensite start (Ms) temperatures were determined for these compositions using predictive machine learning models developed by Agrawal et al. [20] for the determination of Ms temperature.

WAAM Processing

The composition (in wt.%) as quantified by the manufacturers for the P91 steel (ER90S-B91, manufactured by Euroweld, Mooresville, NC, USA) and the 740H superalloy (Special Metals Welding Products Co., Newton, NC, USA) wires that were used for fabricating the graded alloy builds using WAAM are listed in Table 1. The nominal composition of the designed interlayers, namely, 60 and 85% P91

graded alloys determined using the computing the weighted average for each element, is also listed in the same table. The diameter of the P91 steel and 740H superalloy wires were 0.9 and 1 mm, respectively. The builds were fabricated using a robotic WAAM system (ABB robotic platform) in Raytheon Technologies Research Center (RTRC). The system consists of a six-axis robot connected to the twin-wire feeder as well as a plasma arc welding (PAW) torch and the material was deposited over a 12 mm thick mild steel substrate. Purified argon gas was employed for creating the plasma and also used as a shielding gas for the PAW torch with a flow rate of 1.1 L/min to avoid oxidation during deposition. A square wave pattern with a raster pattern width of 11 mm and step-over of 3 mm was used for depositing each layer (Fig. 1) with a constant deposition rate of 0.9 kg/hr. The distance from the torch to the deposition surface and the wire feeding angle were maintained at 15 mm and 30°, respectively.

The printing parameters used for each layer are listed in Table 2. The printing parameters were chosen based on design of experiments for deposition of the constituent materials. Several conditions were tested with various travel speeds, wire feeds, and power, until a stable melt pool was achieved. An average voltage of 20.9 V was maintained during the deposition. The layer height was set as 2 mm for the deposition of P91 steel layers while 1.8 mm for the 740H superalloy. A layer height of ~1.5 mm was maintained for the deposition of the graded alloy. A higher current and lower travel speed as well as wire feed rate were used for the first and

Table 1 Composition (in wt.%) of the P91 and 740H wires used for deposition in the WAAM process and the nominal composition (in wt.%) of 60 and 85% P91 alloy

Material	Composition (wt.%)												
	Al	C	Co	Cr	Cu	Fe	Mn	Mo	Nb	Ni	Ti	Si	V
P91	0.003	0.09	–	9.2	0.03	Bal.	0.45	0.91	0.052	0.4	–	0.26	0.21
740H	1.4	0.03	20.3	24.6	0.02	0.2	0.24	0.5	1.49	Bal	1.5	0.1	–
60% P91	0.56	0.066	8.12	15.4	0.026	53.1	0.37	0.75	0.63	20.1	0.6	0.2	0.13
85% P91	0.21	0.081	3.05	11.5	0.03	75.2	0.42	0.85	0.27	7.8	0.23	0.24	0.18

Fig. 1 Schematic of the tool path used for the fabrication of graded alloy builds using WAAM
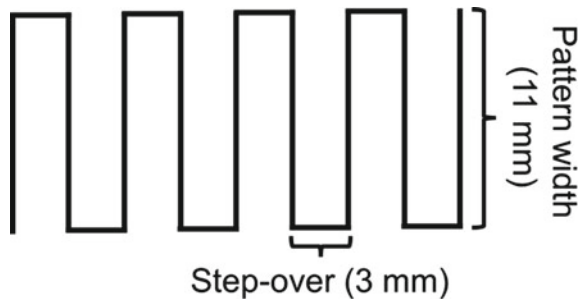
Table 2 Processing parameters for the fabrication of 60 and 85% P91 graded alloy builds using WAAM

Layer no.	Average current (A)	Travel speed (mm/s)	Wire feed (m/min)	Material
60% P91 graded build				
Layer 29–44	166	5	2.44	740H
Layer 13–28	166	5	1.88 P91 0.97 740H	60% P91
Layer 3–12	166	5	3.10	P91
Layer 2	200	4	2.90	P91
Layer 1	220	3.5	2.90	P91
85% P91 graded build				
Layer 29–44	166	5	2.44	740H
Layer 13–28	166	5	2.67 P91 0.37 740H	85% P91
Layer 3–12	166	5	3.10	P91
Layer 2	200	4	2.90	P91
Layer 1	220	3.5	2.90	P91

second layers of P91 steel to ensure good adhesion with the mild steel substrate. The diameter of the P91 steel and 740H superalloy wires, along with their material densities, were used to calculate the relative weight percentage and resulting wire feed values to achieve the desired blends for the graded alloy blocks. The interpass temperature was fixed as 175°C during the deposition. The interpass time for each layer was not fixed and instead it was dictated by the time taken for the sample to cool below 175°C.

Experimental Details

The builds were sectioned along the build (Z) direction, i.e., the XZ plane of the build using electric discharge machining (EDM, Mitsubishi MV2400S, Japan). The sections were ground from 800 to 1200 grit SiC emery papers followed by polishing using suspensions of diamond with particle sizes of 3 and 1 μm as well as colloidal silica with a particle size of 0.04 μm. The as-polished surface was viewed under FEI Scios Dual Beam focused ion beam (FIB)—scanning electron microscope (SEM) attached with a field emission gun (FEG) source. The elemental composition was determined using an energy dispersive spectroscope (EDS, Octane Elite EDS system) attached to the SEM. Detailed phase and grain structure analysis was performed using electron backscattered diffraction (EBSD, EDAX Hickory EBSD system) attached to the SEM, and the data was analyzed further using TSL-OIM software (version 8).

Hardness measurements were carried out using an automated Vicker's micro-hardness tester (AMH55 with LM310AT Microindenter, LECO Corporation, USA)

with a load of 300 g and dwell time of 10 s. Around 400 indentations were made along the build direction (Z direction) to determine the hardness distribution. Flat dog bone-shaped tensile bars (gauge length = 25 mm, total length = 66 mm, width = 5 mm, and thickness = 4 mm) were extracted from the XZ plane of the sample such that both the interfaces are included within the gauge section. Uniaxial tensile tests were carried out with a strain rate of 10^{-3} s^{-1} using MTS 880 universal testing machine with 100 kN capacity. The strain was measured using non-contact digital image correlation (DIC, VIC-2D 7, Correlated Solutions Inc., USA), in order the identify the failure location. The spatial distribution of strains in the gauge section was captured using DIC. The strain was averaged over the complete gauge section and extracted for plotting the stress–strain curves.

Results and Discussion

Computational Design and WAAM Processing

The phase fractions at 760°C predicted using CALPHAD method and the Ms temperatures estimated using machine learning model as a function of the P91 steel content are shown in Fig. 2a and b, respectively. The thermodynamic calculations were performed at 760°C since it is the optimized aging temperature for P91steel and 740H superalloy fabricated using WAAM, based on our previous works [21, 22]. According to the thermodynamic predictions, the matrix phase will have the FCC structure from 0 to 90% P91 and the BCC phase will start to form after 90% P91. Amongst the secondary phases, MX (M: Ti, Nb; X: C) is predicted to form in all the compositions, whereas $M_{23}C_6$ forms only between 83 and 100% P91. Since 740H is a γ′ strengthened superalloy, it appears between 0 and 50% P91 and it is accompanied by σ phase formation from 8 to 45% P91. However, the formation of σ phase is not expected due to the slow diffusion kinetics involved.

The predicted Ms temperature shows a linear trend as a function of P91 content with a small discontinuity close to 60% P91 (Fig. 2b). Two graded alloy compositions, namely, 60 and 85% P91 were identified to test their potential to act as an interlayer between P91 steel and 740H superalloy. Both these compositions are expected to have an FCC matrix structure. However, the calculated Ms temperature of 85% P91 is close to 250°C thus, martensite is expected to form during the cooling process. Since the Ms temperature for the 60% P91 graded alloy is less than room temperature (~15°C), an FCC matrix is expected to form for this composition. In addition, based on the thermodynamic predictions, 85% P91 alloy is expected to be strengthened by the formation of $M_{23}C_6$ precipitates along with the MX phase while the 60% P91 graded alloy will not have any of the major strengthening precipitates except the MX phase.

The graded alloy builds with the designed interlayer composition block sandwiched between the P91 steel and 740H superalloy are shown in Figs. 2c and 2d.
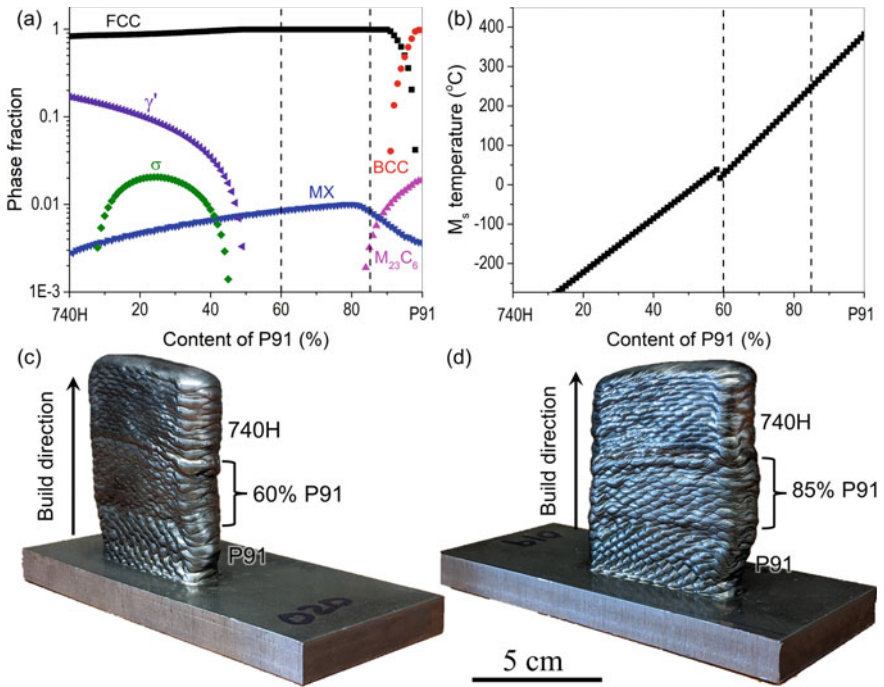
Fig. 2 **a** Phase fraction and **b** Ms temperatures predicted as a function of P91 content. Successful crack-free builds fabricated using WAAM for **c** 60% P91 and **d** 85% P91 graded alloys

The builds were 100 mm long, 10 mm wide, and the total height of the build including the substrate was 87 mm. Different regions of the build were identified based on the differences in the melt pool size as seen from the lateral sides of the build. These builds were intended to be deposited for a total ideal height of nearly 77 mm from the substrate with an ideal height of 24, 24, and 28.8 mm for P91 steel, graded alloy, and 740H superalloy, respectively. The measured heights of each block were ~21 mm for P91 steel, 24 mm for 60 and 85% P91 graded alloys, and ~29 mm for the 740H superalloy with a total height close to 74 mm which is very close to the ideal height of the build. Since the first two layers of P91 steel were mixed completely with the substrate for good adhesion, the height of the P91 steel block was slightly smaller than the ideal height. Hence, the interpass temperature (175°C) used for depositing these builds has been effective in reducing the dilution between the layers.

The composition of the 60 and 85% P91 graded alloy builds along the build direction of the sample measured using EDS is shown in Fig. 3a and b. It was observed that the measured composition of the graded alloy interlayer is close to the nominal composition listed in Table 1. This proves that WAAM is a robust AM technique to deposit a graded alloy using the twin-wire feeder. Moreover, it can be clearly seen that Fe and Ni concentration spikes downward throughout the graded alloy and 740H superalloy regions along with a simultaneous increase in the composition of Mo, Nb,

or Ti. Further EDS mapping confirms the presence of secondary phases in the graded alloy blocks as shown in Fig. 3c and d. From Fig. 3(c1–c4) it is evident that the bright phase with irregular structure is rich in Nb, Mo, and Ti, which corresponds to the Laves phase. Figures 3(d1–d3) shows that the dark square-shaped phase has a high content of Ti and a moderate amount of Nb which can be correlated with the MC carbide.

The inverse pole figure (IPF) and phase maps obtained using EBSD for the 60 and 85% P91 alloys are shown in Fig. 4. From the phase maps shown in Fig. 4b and d, it can be found that the 60% P91 graded alloy has a matrix with FCC structure while the 85% P91 alloy has a martensitic structure. This proves that the Ms temperature prediction matches well with the experimental observation for the designed graded alloys. Moreover, a coarse-grained microstructure with no particular texture was observed in the 60% P91 graded alloy, as shown in Fig. 4a, which could be possibly due to the multiple heating and cooling cycles underwent during the deposition. In the 85% P91 graded alloy (Fig. 4b), a clear partition was observed, where one side
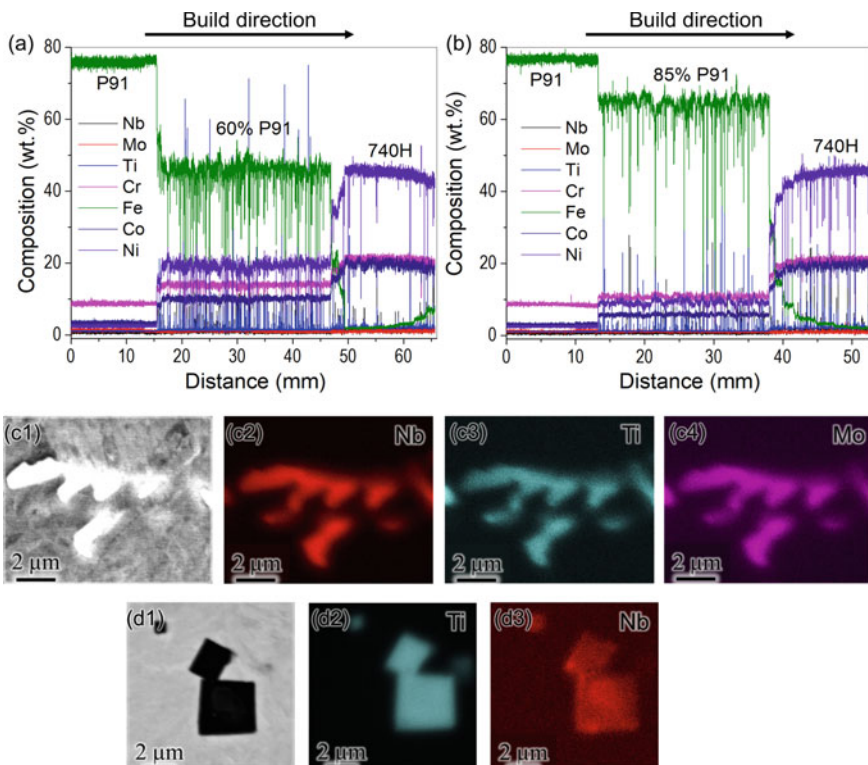
Fig. 3 Composition profile along the build direction determined using EDS for **a** 60 and **b** 85% P91 graded alloy blocks. Compositions profiles for **c1–c4** Laves phase and **d1–d3** MC carbide obtained using area EDS mapping showing that the Laves phase is rich in Mo, Nb, and Ti while the MC carbide is rich in Ti and Nb, respectively
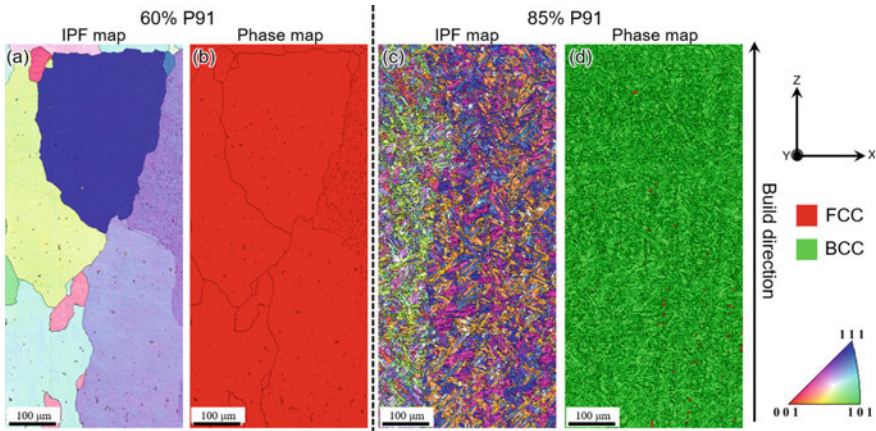
Fig. 4 IPF and phase maps obtained using EBSD for **a**, **b** 60% and **c**, **d** 85% P91 graded alloy blocks showing a coarse-grained FCC structure for the 60% P91 alloy and a fine martensitic structure for the 85% P91 alloy

had grains mostly oriented between (111) and (001) planes (blue, pink, and orange grains, refer to IPF color map) while the other side had grains oriented mostly close to (101) plane (green grains, refer to IPF color map). Hence, the partition between these two types of grains signifies the presence of a prior austenite grain boundary.

The hardness maps obtained along the build direction in the XZ plane of the graded alloys builds are shown in Fig. 5. The hardness of 60% P91 graded alloy is very low in comparison with the pure P91 steel and 740H superalloy. On the other hand, the hardness is predominantly uniform along the build direction for the 85% P91 alloy and the average hardness is higher than the corresponding value for the 60% P91 graded alloy. The striking difference between the hardness of 60 and 85% P91-graded alloys can be attributed to the microstructure of the matrix phase in these alloys. The 60% P91 alloy consists of an FCC phase structure which is generally softer than the martensitic matrix found in the 85% P91 alloy. The 60% P91 alloy has coarse grains, whereas the 85% P91 alloy has a fine martensitic structure (Fig. 4). In addition to the hardness of the graded alloy blocks, there were other weak and strong regions that could be observed from the hardness maps. In the 60% P91 graded alloy build (Fig. 5a), the P91 steel close to the interface between P91 steel and 60% P91 alloy is much higher in comparison with the same material away from the interface. Similarly, a region of low hardness was identified at the interface between 85% P91 alloy and 740H superalloy, as seen in Fig. 5b.

In order to probe into the reason for the formation of harder P91 steel close to the 60% P91 alloy and a weak region between 85% P91and 740H superalloy, further microstructure analysis was performed using EBSD and the IPF and phase maps from these regions are shown in Fig. 6. The IPF and phase maps from the interface between P91 steel and 60% P91 alloy show that the martensite in the P91 steel region is very fine (Fig. 6a and b) in comparison with the P91 steel farther away from the
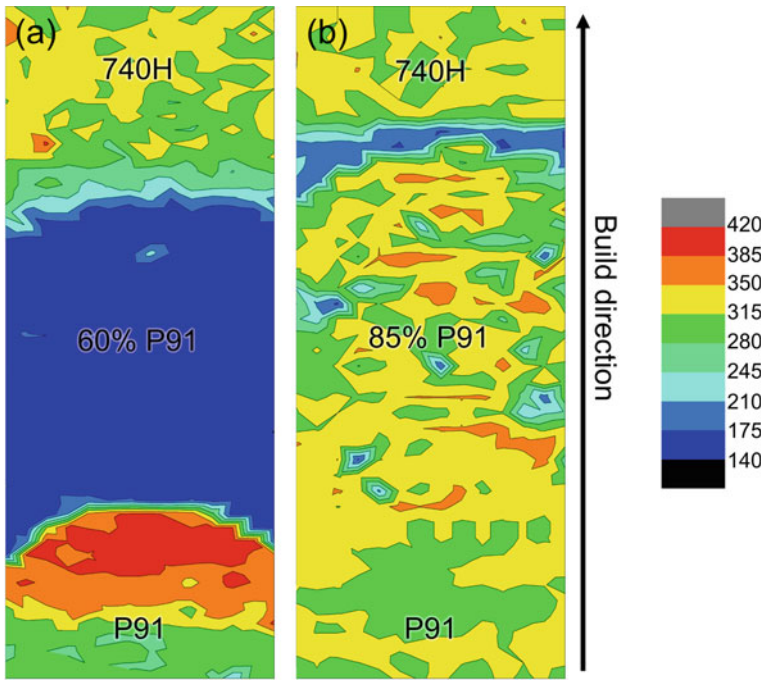
Fig. 5 Hardness maps obtained along the build direction in the XZ plane of **a** 60% and **b** 85% P91 graded alloy. The length and width of the hardness maps are 40 and 11 mm, respectively. The color bar corresponds to the hardness in $HV_{0.3}$

interface where the martensite grains are coarser as it can be seen from Fig. 6c and d. The difference in the grain structure of the P91 steel, near and away from the interface can be attributed to the cyclic re-austenitization of the martensite. When the first few layers of 60% P91 alloy are deposited over the previously deposited P91 steel, the temperature of the P91 steel close to the interface increases to the extent that the martensite can undergo re-austenitization followed by cooling to form refined martensite. It has been demonstrated in our previous work [23] that cyclic re-austenitization in steels can lead to refinement of martensite with increase in hardness. From the IPF and phase maps obtained from the interface between 85% P91 alloy and 740H superalloy (Fig. 6e and f), a band of two-phase region consisting of martensite from 85% P91 alloy and γ phase from 740H superalloy is clearly visible. Hence, the region with low hardness at the interface between 85% P91 alloy and 740H superalloy can be attributed to the difference in the matrix phase structure of the two alloys leading to the formation of a mixture of martensite and γ phases.
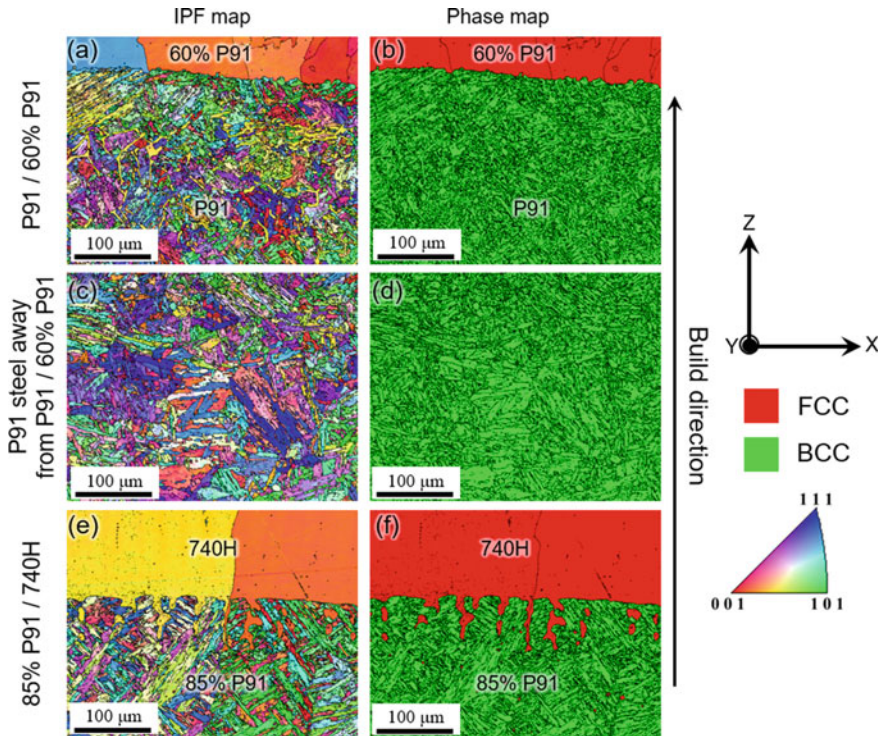
Fig. 6 IPF and phase maps obtained using EBSD at **a**, **b** interface between P91 steel and 60% P91 graded alloy, **c**, **d** P91 steel farther away from the interface between P91 steel and 60% P91 graded alloy and **e**, **f** interface between 85% P91 graded alloy and 740H superalloy

Design of Post-heat Treatment and Mechanical Testing

A two-step post-heat treatment comprising of homogenization and aging was adopted where the homogenization step will dissolve the secondary phases and relieve the residual stresses, whereas the aging step will induce the precipitation of the strengthening phases. The calculated phase fractions as a function of temperature for the 60 and 85% P91 graded alloy composition listed in Table 1 are shown in Fig. 7. The homogenization temperature was identified as 1150°C since all the secondary phases except MX will dissolve at this temperature based on the predicted phase fractions. The homogenization time was chosen to be 1 h because a longer time period can lead to grain growth at high temperatures. Hence, the homogenization for the graded alloy builds was performed at 1150°C for 1 h followed by water quenching.

The aging temperature of 760°C was found to be suitable because at that temperature the fraction of MX in 60% P91 alloy and the fractions of $M_{23}C_6$ as well as MX phases in 85% P91 alloy were found to be maximum based on the thermodynamic predictions. In addition, 760°C was identified as the optimum aging temperature for
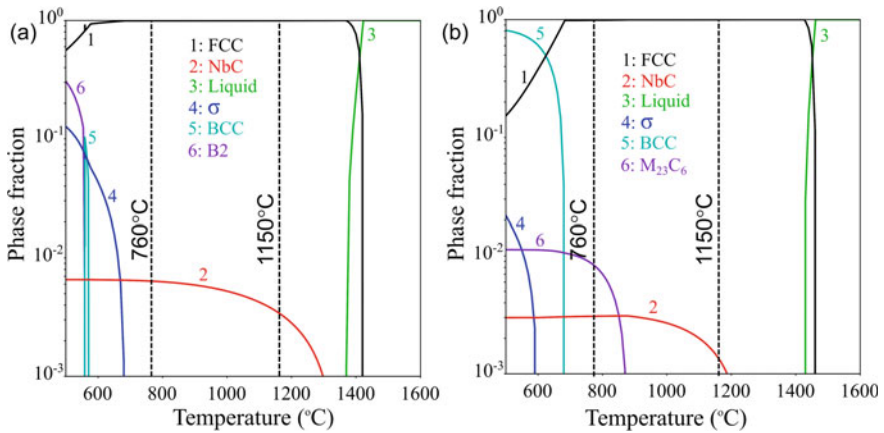
Fig. 7 Fraction of phases as a function of temperature predicted using thermodynamic calculations for **a** 60% and **b** 85% P91 graded alloys

P91 steel [21] and 740H superalloy [22] and moreover, different aging temperatures cannot be used for a multi-material build, as mentioned previously. In order to identify the optimum aging time, the samples were subjected to aging heat treatment after homogenization for different times at 760°C followed by air cooling. The time durations for aging were identified as 2, 4, 8, and 12 h because the optimum aging time for P91 steel [21] and 740H superalloy [22] are 2 and 12 h, respectively. Two time periods were chosen in between (4 and 8 h) in order to identify the optimal condition.

In order to identify the optimum aging time, the peak hardness needs to be determined. The hardness maps obtained for different aging times at 760°C for 60 and 85% P91 graded alloy builds are shown in Figs. 8 and 9, respectively. The hardness maps for aged 60% P91 builds showed no improvement in hardness after aging (Fig. 8). This observation agrees well with the CALPHAD calculations which predicted a lack of strengthening precipitates at 760°C. This proves that there is a good correlation between the CALPHAD predictions and experimental observations. On the contrary, the hardness of the 85% P91 graded alloy sample improved significantly after aging as shown in Fig. 9. The width of the soft zone, which is a mixture of martensite and γ phases (Fig. 6f), was found to be unchanged after 2 h of aging while reduced slightly after aging for 4 h. After aging for 8 and 12 h, the soft zone width reduced considerably showing that a longer aging time is required to allow the diffusion. However, as the aging time is increased, the pure P91 steel becomes weaker with low hardness since it has reached an overaged condition. Thus, the optimum aging time was identified as 8 h at 760°C to attain reduced width of the soft zone without lowering the hardness of pure P91 steel extensively.

The stress–strain curves and the tensile properties obtained after mechanical testing equipped with DIC are shown in Fig. 10 and Table 3, respectively. No significant improvement was observed in the yield strength and ultimate tensile strength of
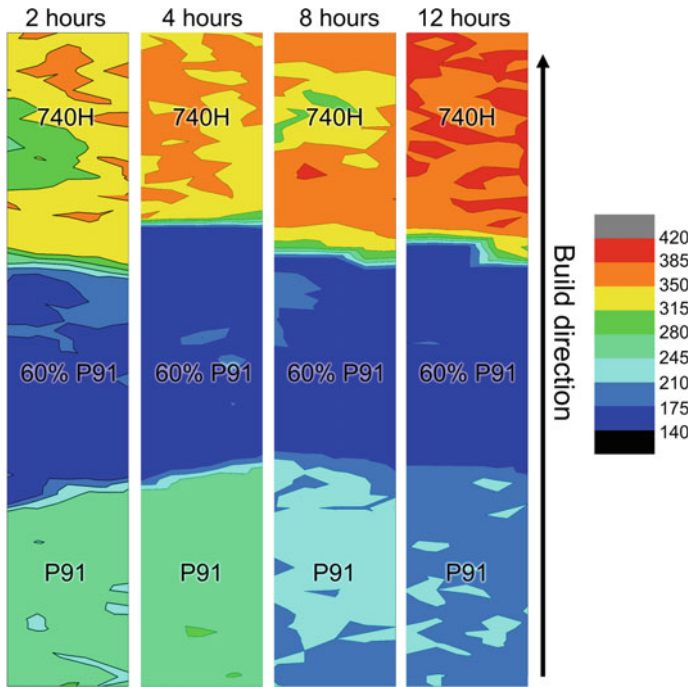
Fig. 8 Hardness maps for 60% P91 graded alloy after aging at 760°C for different durations. The length and width of the hardness maps are 50 and 4 mm, respectively. The color bar corresponds to the hardness in $HV_{0.3}$

the heat treated 60% P91 graded alloy builds. However, the ductility of the as-built alloy is higher than the heat treated 60% P91 graded alloy possibly due to the precipitation of the fine and brittle MC carbides during aging which can act as crack initiation sites. On the other hand, there is a considerable improvement in the yield strength and ductility of 85% P91 graded alloy build after post-heat treatment (Table 3). The precipitation of $M_{23}C_6$ precipitates could have contributed to the strengthening of the graded alloy and hence, enhanced tensile properties has been achieved.

In addition, DIC was used to calculate the strains during the mechanical testing to identify the region where the necking starts. The locations of failure (region enclosed by a white rectangle) identified from screenshots of the strain map are shown in Fig. 11. The 60% P91 graded alloy failed in the graded alloy block in as-built and heat treated conditions since the strength did not improve with the application of post-heat treatment (Fig. 11a and b). However, the location of failure changed with application of post-heat treatment for the 85% P91 graded alloy. In the as-built condition, the sample failed at the interface between the 85% P91 alloy and 740H superalloy as shown in Fig. 11(c) since the hardness in this region was low due to the presence of a two-phase region with martensite and γ phases. After post-heat treatment, the location of failure shifted to the pure P91 block (Fig. 11(d)). The failure in the pure
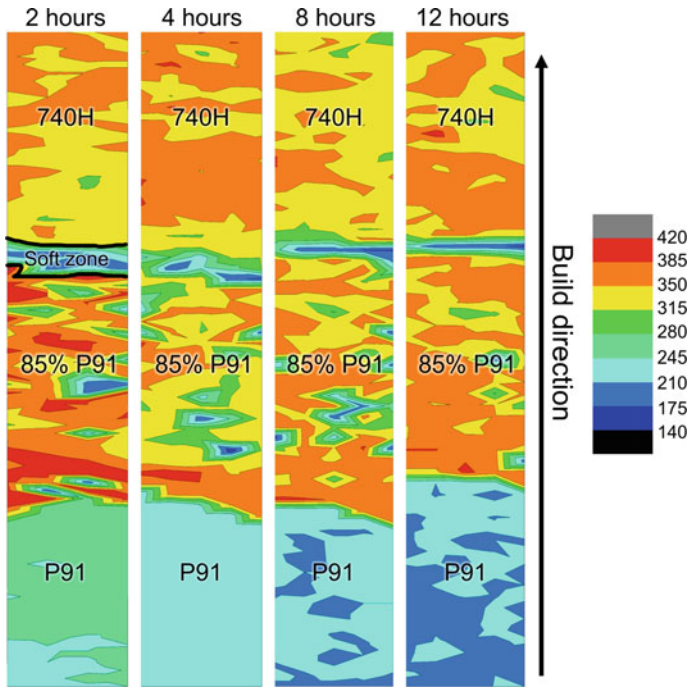
Fig. 9 Hardness maps for 85% P91 graded alloy after aging at 760°C for different durations. The length and width of the hardness maps are 50 and 4 mm, respectively. The color bar corresponds to the hardness in $HV_{0.3}$

P91 region is inevitable since it would have reached an overaged condition as the optimum aging time for this material is 2 h [21]. Therefore, the designed post-heat treatment for the 85% P91 graded alloy has strengthened the material to achieve improved mechanical performance.

Conclusions

A CALPHAD-based ICME framework has been employed to design the composition of the graded alloy that can potentially act as an interlayer between P91 steel and 740H superalloy. The designed compositions were fabricated using WAAM along with microstructure characterization and mechanical property testing. The salient outcomes from the present study can be summarized as follows.

- Guided by the high-throughput calculations, the bimetallic alloy builds with 60 and 85% P91 as interlayers were fabricated successfully with desired composition and reduced dilution using WAAM.
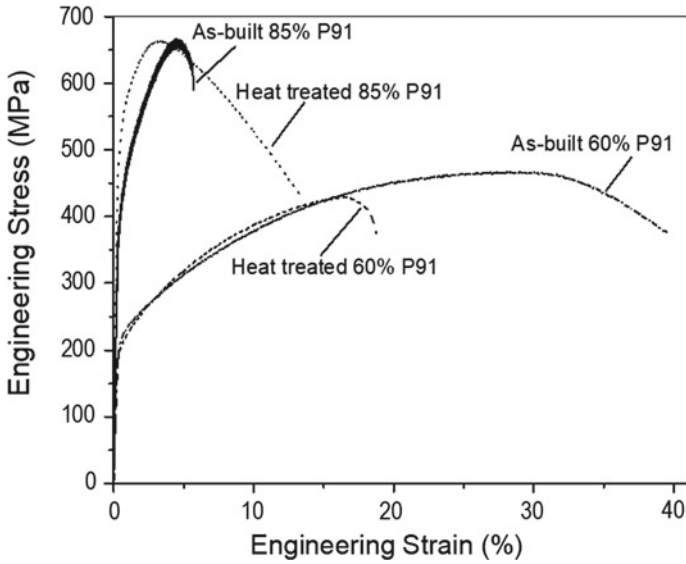
Fig. 10 Stress–Strain curves obtained using mechanical testing equipped with DIC for 60 and 85% P91 graded alloys builds in as-built and heat treated conditions

Table 3 Tensile properties and failure locations for 60 and 85% P91 builds fabricated using WAAM in different conditions (2 samples were tested for each condition to determine the standard deviation)

Material	Condition	Yield strength (MPa)	Ultimate tensile strength (MPa)	Elongation (%)	Location of failure
60% P91	As-built	219 ± 2	459 ± 11	32.5 ± 9.9	60% P91 block
	Heat treated	212 ± 2	440 ± 14	21.2 ± 3.1	60% P91 block
85% P91	As-built	419 ± 5	665 ± 18	6.5 ± 1.2	Interface between 85% P91 and 740H blocks
	Heat treated	538 ± 22	667 ± 6	13.2 ± 0.1	P91 block

- The matrix of 60% P91 alloy had a coarse-grained FCC structure, while the 85% P91 alloy comprises a fine-grained martensitic matrix and secondary phases such as the Laves phase and MC carbides. There is a good correlation between the predicted phases and the observed microstructure in the WAAM builds.
- The hardness of 60% P91 graded alloy is much lower than the 85% P91 alloy. Moreover, the interface between the 85% P91 alloy and 740H superalloy is low due to the presence of a two-phase mixture of martensite and γ phases, while the fine martensitic structure of the P91 steel close to the interface between P91 steel and 60% P91 alloy increased its hardness.

Fig. 11 Location of failure identified using the DIC strain maps for **a**, **b** 60% and **c**, **d** 85% P91 graded alloy builds in as-built and heat treated conditions. The color bar corresponds to the strain in %
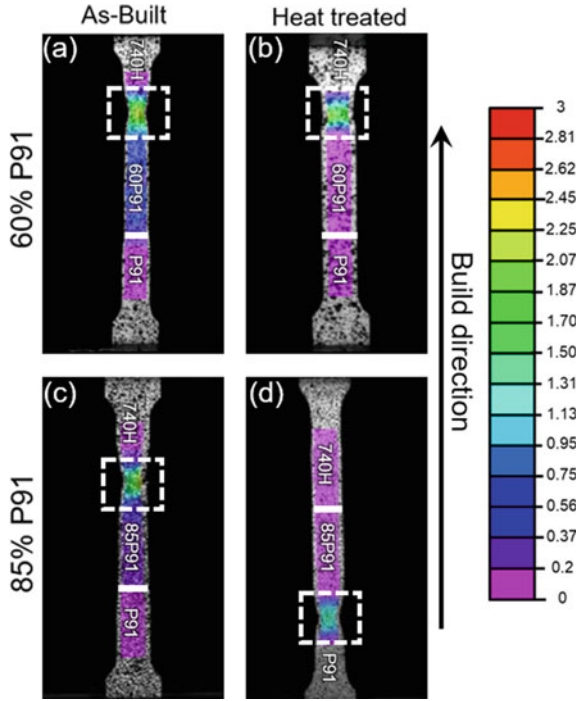
- 60% P91 graded alloy showed no improvement in the hardness even after applying the post-heat treatment due to lack of effective strengthening precipitates, while 85% P91 graded alloy showed considerable improvement in the hardness after aging with an optimum aging time of 8 h.
- The location of failure for the 60% P91 graded alloy remained within the graded alloy block in as-built and heat treated conditions whereas the as-built 85% P91 graded alloy build failed at the interface between the intermediate block and 740H superalloy interface and it shifted to the pure P91 after the post-heat treatment.
- This work demonstrated that the CALPHAD-based ICME design frame is essential for the successful bimetallic printing using the WAAM combined with post-heat treatment.

otherwise does not necessarily constitute or imply its endorsement, recommendation, or favoring by the United States Government or any agency thereof. The views and opinions of authors expressed herein do not necessarily state or reflect those of the United States Government or any agency thereof.

References

1. De Barbadillo JJ, Baker BA, Virginia W (2014) Microstructure stability of Alloy 740H and its effect on material properties. Proceedings of the ASME Symposium on Elevated Temperature Application of Materials for Fossil, Nuclear and Petrochemical Industries, 1–13.
2. Pandey C, Giri A, Mahapatra MM (2016) Evolution of phases in P91 steel in various heat treatment conditions and their effect on microstructure stability and mechanical properties. Mater. Sci. Eng. A. 664:58–74. https://doi.org/10.1016/j.msea.2016.03.132.
3. Sun Z, Karppi R (1996) The application of electron beam welding for the joining of dissimilar metals: An overview. J. Mater. Process. Technol. 59:257–267. https://doi.org/10.1016/0924-0136(95)02150-7.
4. Xue P, Ni DR, Wang D, Xiao BL, Ma ZY (2011) Effect of friction stir welding parameters on the microstructure and mechanical properties of the dissimilar Al-Cu joints. Mater. Sci. Eng. A. 528:4683–4689. https://doi.org/10.1016/j.msea.2011.02.067.
5. Feng J, Songbai X, Wei D (2012) Reliability studies of Cu/Al joints brazed with Zn-Al-Ce filler metals. Mater. Des. 42:156–163. https://doi.org/10.1016/j.matdes.2012.05.028.
6. Guo Y, Liu G, Jin H, Shi Z, Qiao G (2011) Intermetallic phase formation in diffusion-bonded Cu/Al laminates. J. Mater. Sci. 46:2467–2473. https://doi.org/10.1007/s10853-010-5093-0.
7. Onuike B, Heer B, Bandyopadhyay A (2018) Additive manufacturing of Inconel 718—Copper alloy bimetallic structure using laser engineered net shaping (LENS^{TM}). Addit. Manuf. 21:133–140. https://doi.org/10.1016/j.addma.2018.02.007.
8. Gorsse S, Hutchinson C, Gouné M, Banerjee R (2017) Additive manufacturing of metals: a brief review of the characteristic microstructures and properties of steels, Ti-6Al-4V and high-entropy alloys. Sci. Technol. Adv. Mater. 18:584–610. https://doi.org/10.1080/14686996.2017.1361305.
9. Herzog D, Seyda V, Wycisk E, Emmelmann C (2016) Additive manufacturing of metals. Acta Mater. 117:371–392. https://doi.org/10.1016/J.ACTAMAT.2016.07.019.
10. Imran MK, Masood SH, Brandt M, Bhattacharya S, Mazumder J (2011) Direct metal deposition (DMD) of H13 tool steel on copper alloy substrate: Evaluation of mechanical properties. Mater. Sci. Eng. A. 528:3342–3349. https://doi.org/10.1016/j.msea.2010.12.099.
11. Domack MS, Baughman JM (2005) Development of nickel-titanium graded composition components. Rapid Prototyp. J. 11:41–51. https://doi.org/10.1108/13552540510573383.
12. Sahasrabudhe H, Harrison R, Carpenter C, Bandyopadhyay A (2015) Stainless steel to titanium bimetallic structure using LENS^{TM}. Addit. Manuf. 5:1–8. https://doi.org/10.1016/j.addma.2014.10.002.
13. Carroll BE, Otis RA, Borgonia JP, Suh, JO Dillon RP, Shapiro AA, Hofmann DC, Liu ZK, Beese AM (2016) Functionally graded material of 304L stainless steel and inconel 625 fabricated by directed energy deposition: Characterization and thermodynamic modeling. Acta Mater. 108:46–54. https://doi.org/10.1016/j.actamat.2016.02.019.
14. Ali H, Ghadbeigi H, Mumtaz K (2018) Processing Parameter Effects on Residual Stress and Mechanical Properties of Selective Laser Melted Ti6Al4V. J. Mater. Eng. Perform. 27:4059–4068. https://doi.org/10.1007/S11665-018-3477-5/FIGURES/19.
15. Hauser T, Reisch RT, Seebauer S, Parasar A, Kamps T, Casati R, Volpp J, Kaplan AFH (2021) Multi-Material Wire Arc Additive Manufacturing of low and high alloyed aluminium alloys with in-situ material analysis. J. Manuf. Process. 69:378–390. https://doi.org/10.1016/J.JMAPRO.2021.08.005.

16. Chang T, Fang X, Liu G, Zhang H, Huang K (2022) Wire and arc additive manufacturing of dissimilar 2319 and 5B06 aluminum alloys. J. Mater. Sci. Technol. 124:65–75. https://doi.org/10.1016/J.JMST.2022.02.024.

17. Ahsan MRU, Tanvir ANM, Ross T, Elsawy A, Oh MS, Kim DB (2019) Fabrication of bimetallic additively manufactured structure (BAMS) of low carbon steel and 316L austenitic stainless steel with wire + arc additive manufacturing. Rapid Prototyp. J. 26:519–530. https://doi.org/10.1108/RPJ-09-2018-0235.

18. Mohan Kumar S, Rajesh Kannan A, Pravin Kumar N, Pramod R, Siva Shanmugam N, Vishnu AS, Channabasavanna SG (2021) Microstructural Features and Mechanical Integrity of Wire Arc Additive Manufactured SS321/Inconel 625 Functionally Gradient Material. J. Mater. Eng. Perform. 30:5692–5703. https://doi.org/10.1007/S11665-021-05617-3/FIGURES/13.

19. Sridar S, Klecka MA, Xiong W (2022) Interfacial characteristics of P91 steel - Inconel 740H bimetallic structure fabricated using wire-arc additive manufacturing. J. Mater. Process. Technol. 300:117396. https://doi.org/10.1016/J.JMATPROTEC.2021.117396.

20. Agrawal A, Saboo A, Xiong W, Olson G, Choudhary A (2019) Martensite start temperature predictor for steels using ensemble data mining. 2019 IEEE International Conference on Data Science and Advanced Analytics (DSAA), 521–530. https://doi.org/10.1109/DSAA.2019.00067.

21. Li K, Klecka MA, Chen S, Xiong W (2021) Wire-arc additive manufacturing and post-heat treatment optimization on microstructure and mechanical properties of Grade 91 steel. Addit. Manuf. 37:101734. https://doi.org/10.1016/J.ADDMA.2020.101734.

22. Sridar S, Klecka MA, Xiong W (2022) Effect of post-deposition heat treatment on the microstructure and mechanical properties of Inconel 740H fabricated using wire-arc additive manufacturing (Unpublished work).

23. Sridar S, Zhao Y, Xiong W (2020) Cyclic re-austenitization of copper-bearing high-strength low-alloy steels fabricated by laser powder bed fusion, Mat. Char. 166:110437. https://doi.org/10.1016/j.matchar.2020.110437.

SUPERALLOY 718 and Derivatives

EDITORS:

Eric A. Ott
Joel Andersson
Chantal Sudbrack
Zhongnan Bi
Kevin Bockenstedt
Ian Dempster
Michael Fahrmann
Paul Jablonski
Michael Kirka
Xingbo Liu
Daisuke Nagahama
Tim Smith
Martin Stockinger
Andrew Wessman

TMS

Springer

The Minerals, Metals & Materials Series

Eric A. Ott · Joel Andersson · Chantal Sudbrack ·
Zhongnan Bi · Kevin Bockenstedt · Ian Dempster ·
Michael Fahrmann · Paul Jablonski ·
Michael Kirka · Xingbo Liu · Daisuke Nagahama ·
Tim Smith · Martin Stockinger · Andrew Wessman
Editors

Proceedings of the 10th International Symposium on Superalloy 718 and Derivatives

TMS

Springer

Editors
Eric A. Ott
General Electric
Cincinnati, OH, USA

Chantal Sudbrack
National Energy Technology Laboratory
Albany, OR, USA

Kevin Bockenstedt
ATI Specialty Materials
Monroe, NC, USA

Michael Fahrmann
Haynes International
Kokomo, IN, USA

Michael Kirka
Oak Ridge National Laboratory
Oak Ridge, TN, USA

Daisuke Nagahama
Honda R&D Co., Ltd.
Wakō, Saitama, Japan

Martin Stockinger
Montanuniversität Leoben
Leoben, Austria

Joel Andersson
University West
Trollhättan, Sweden

Zhongnan Bi
Central Iron and Steel Research Institute
Beijing, China

Ian Dempster
Wyman Gordon/PPC
Houston, TX, USA

Paul Jablonski
National Energy Technology Laboratory
Albany, OR, USA

Xingbo Liu
West Virginia University
Morgantown, WV, USA

Tim Smith
NASA Glenn Research Center
Cleveland, OH, USA

Andrew Wessman
The University of Arizona
Tucson, AZ, USA